DOI: 10.1002/ ((please add manuscript number))

Article type: Full Paper

Title: Charge Generation and Recombination in an Organic Solar Cell with Low Energetic Offsets

Niva A. Ran,[1] John A. Love,[1,2] Michael C. Heiber,[1] Xuechen Jiao,[3] Michael P. Hughes,[1] Akchheta Karki,[1] Ming Wang,[1] Viktor V. Brus,[1,4] Hengbin Wang,[5] Dieter Neher,[2] Harald Ade,[3] Guillermo C. Bazan,[,1] Thuc-Quyen Nguyen*[,1]*

[1] NAR, JAL, MCH, MPH, AK, MW, VB, GCB, TQN

Center for Polymers and Organic Solids, University of California, Santa Barbara, California 93106, United States

[2] JAL, DN

Institute of Physics and Astronomy, University of Potsdam, 14476 Potsdam, Germany

[3] XJ, HA

Department of Physics and Organic and Carbon Electronics Lab (ORaCEL), North Carolina State University, Raleigh, NC 27695, United States

[4] VB

Helmholtz-Zentrum Berlin für Materialien und Energie GmbH, Institut für Silizium Photovoltaik, Kekuléstr. 5, 12489 Berlin, Germany

[5] HW

Mitsubishi Chemical Center for Advanced Materials, University of California, Santa Barbara, California 93106, United States

E-mail: bazan@chem.ucsb.edu, quyen@chem.ucsb.edu

Keywords: organic solar cells, recombination, energetic offset, fill factor, morphology

Abstract

Organic bulk heterojunction (BHJ) solar cells require energetic offsets between the donor and acceptor to obtain high short circuit currents (J_{SC}) and fill factors (*FF*). However, it is necessary to reduce the energetic offsets to achieve high open-circuit voltages (V_{OC}). Recently, reports have highlighted BHJ blends which are pushing at the accepted limits of energetic offsets necessary for high efficiency. Unfortunately, most of these BHJs have modest *FF* values. How the energetic offset impacts the solar cell characteristics thus remains poorly understood. Here, we report a comprehensive characterization of the losses in a polymer:fullerene BHJ blend, PIPCP:$PC_{61}BM$, that achieves a high V_{OC} (0.9 V) with very low energy losses (E_{loss}=0.52 eV) from the energy of absorbed photons, a respectable J_{SC} (13 mA/cm^2), but a limited *FF* (54%). Despite the low energetic offset, the system does not suffer from field-dependent generation, and instead it is characterized by very fast non-geminate recombination and the presence of shallow traps. The charge carrier losses are attributed to suboptimal morphology due to high miscibility between PIPCP and $PC_{61}BM$. These results hold promise that given the appropriate morphology, the J_{SC}, V_{OC}, and *FF* can all be improved, even with very low energetic offsets.

1. Introduction

Studies on organic bulk heterojunction (BHJ) photovoltaics (OPV) have suggested that if the energetic offset between donor and acceptor electron (or hole) transport levels is below 100-300 meV, the efficiency of charge generation and extraction is severely diminished, resulting in decreased short circuit currents (J_{SC}) and fill factors (*FF*).[1,2] Recently, a number of groups have reported BHJ blends that are pushing at the accepted limits of energetic offsets necessary for efficient solar cell devices.[3–7] Active layers with low energetic offsets are desirable in order to achieve solar cells with high open-circuit voltages (V_{OC}). However, most of these blends are only able to achieve modest *FF* values.[5–7]

The *FF* is a parameter used to describe the efficiency of charge generation and collection across the operating voltages of the solar cell. In the absence of charge recombination losses, the *FF* is only limited by the series and shunt (parallel) resistances in the solar cell device,[8] as is the case for inorganic solar cells where the *FF* can achieve values above 80%. However, in OPVs charge generation and extraction are known to be hindered by geminate and/or non-geminate (specifically, bimolecular) charge recombination losses, and thus the *FF* of OPVs is often lower.[9–11] As a consequence of these recombination losses, the operation of organic solar cells can be described as a field-dependent competition between charge extraction and charge recombination.[12–15] In recent years there have been some reports on organic solar cells that achieve very impressive *FF* values, approaching 80%.[16–22]

Although a simplified description, the V_{OC} and the J_{SC} are determined by the hole and electron quasi-Fermi level separation. The efficiency of the solar cell to absorb photons and generate photocurrent under the internal field of the device is described by the external quantum efficiency, EQE. Recently, we have introduced a low-bandgap regioregular polymer, PIPCP (**Figure 1a**), that can achieve a high V_{OC} in BHJ solar cells when blended with the electron acceptor phenyl-C61-butyric acid methyl ester ($PC_{61}BM$).[23] PIPCP contains a backbone comprised of CPDT-PT-IDT-PT repeat units

(CPDT=cyclopentadithiophene, PT=pyridyl[2,1,3]thiadiazole, IDT=indacenodithiophene) and strictly organized PT orientations, such that the pyridyl N-atoms point toward the CPDT fragment. The energy loss, E_{loss}, defined as the difference between the polymer bandgap (E_g) and the V_{OC}, $E_{loss} = E_g - qV_{OC}$, was determined to be among the lowest losses reported in the literature (0.52 eV), for a system with a PCE > 6% (the PCE of PIPCP:PC_{61}BM is PCE = 6.4% ± 0.3%). The low E_{loss} was attributed to a minimal offset between the E_g and the charge transfer (CT) state energy (E_{CT}), E_g - $E_{CT} \leq 50$ meV. However, the *FF* of PIPCP:PC_{61}BM BHJs has remained low, at ≈54%, despite multiple attempts at device optimization.[6] Given that this blend system is pushing the accepted limits of operational OPVs,[7] we asked: why is the *FF* in PIPCP:PC_{61}BM low and is this a direct consequence of the low energetic offset? Answering these questions has fundamental importance for the field of organic photovoltaics.

In the remainder of this manuscript we investigate possible reasons for the low *FF* in PIPCP:PC_{61}BM blends. Our results indicate that charge generation in PIPCP:PC_{61}BM is not field-dependent. Instead, we find that the low *FF* in PIPCP:PC_{61}BM solar cells may be explained by very fast non-geminate recombination. Importantly, we find that the blend films of PIPCP:PC_{61}BM blend films are characterized by an intimately mixed morphology, which can explain the fast non-geminate recombination. Indeed, bilayers of PIPCP/C_{60} have a much higher *FF* = 72%, which drops significantly to 56% upon thermal annealing, emphasizing the detrimental impact of a poor morphology between PIPCP and fullerenes. Finally, we remain hopeful about the possibility of achieving high PCE values using organic solar cells with low E_{loss} values, given a good morphology.

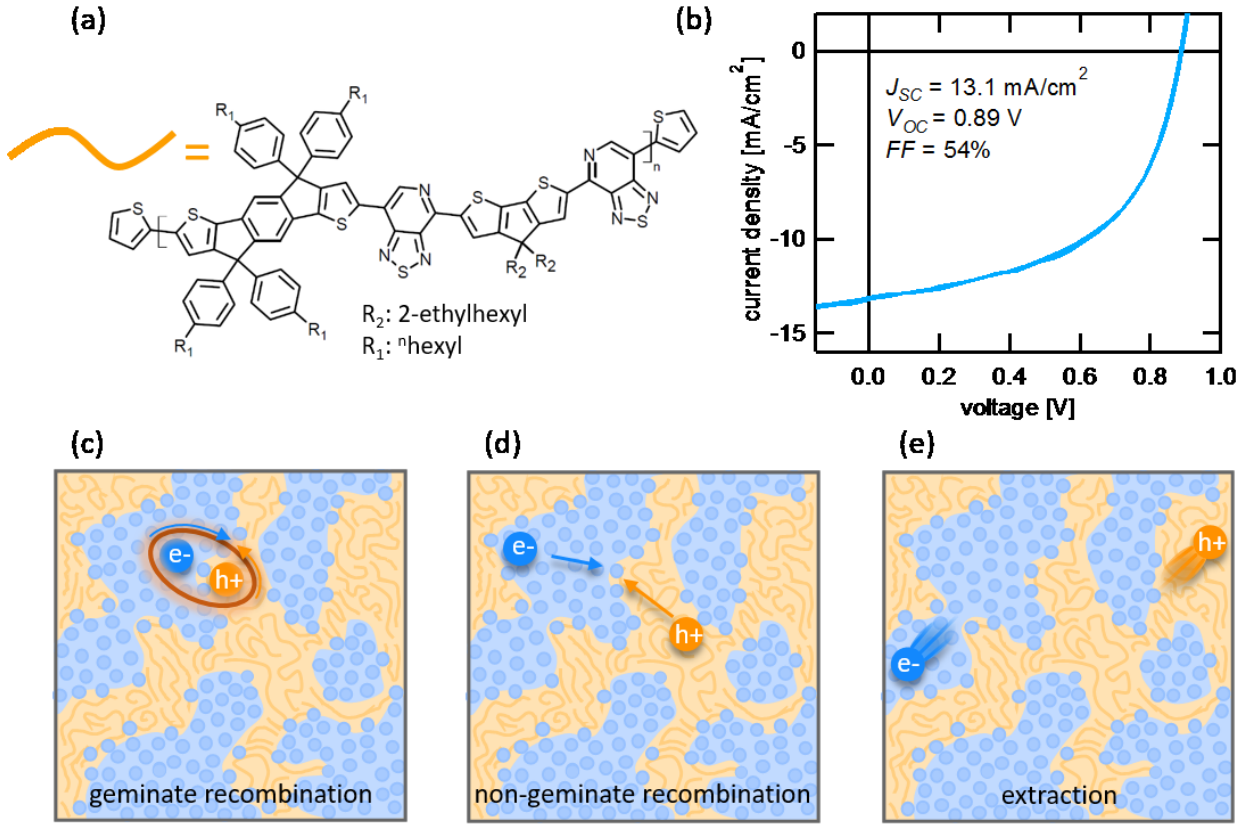

Figure 1. (a) Molecular structure of PIPCP. (b) *J-V* characteristics of PIPCP:$PC_{61}BM$ BHJ solar cells under 1-sun illumination. Schematic representation of (c) geminate recombination, (d) non-geminate recombination, and (e) charge extraction.

2. Results and Discussion

Figure 1b shows a characteristic current-voltage (*J-V)* curve for a PIPCP:$PC_{61}BM$ BHJ solar cell under 1 sun illumination with a high V_{OC} = 0.89 V but limited *FF* = 54%. The low *FF* denotes that as the field across the active layer decreases (*i.e.* the applied bias approaches V_{OC}), the balance between charge recombination and charge extraction shifts towards recombination losses. It has been suggested that the low energetic driving force for charge separation in PIPCP:$PC_{61}BM$ may give rise to field-dependent generation, thus reducing the *FF*.[6] On the other hand, Menke *et al.* have

shown that PIPCP:$PC_{61}BM$ blends are characterized by fast triplet formation from the charge transfer (CT) state.[24] Since this process opens a new channel for CT state recombination, while also competing with CT state re-splitting into free carriers, more significant bimolecular recombination and poor charge extraction has been suggested.[24] As described below, here we explore the possible effects of contact limitations, report new insights on the blend morphology, and determine the contributions of geminate recombination, non-geminate recombination, temperature and charge transport, from the point of view of limitations on the *FF* of PIPCP:$PC_{61}BM$. Geminate recombination, non-geminate recombination, and charge extraction are schematically represented in **Figure 1c-e**.

2.1. Ruling Out Contact Limitations

Non-Ohmic contacts may cause a reduced electric field and space-charge buildup, which would lead to increased charge recombination.[25–28] To ensure that the *FF* in PIPCP:$PC_{61}BM$ solar cells is not limited by extraction barriers at the contacts, we fabricated PIPCP:$PC_{61}BM$ solar cells with various device architectures. Inverted solar cells were fabricated with zinc oxide and PEIE as the bottom contact (cathode), and silver-capped molybdenum oxide as the top contact (anode). Regular solar cells were fabricated with PEDOT:PSS and molybdenum oxide as the bottom contacts (anode), topped with calcium, lithium fluoride, and bathocuporoine capped with aluminum. Despite the various architectures, there was no improvement in device performance. The 1-sun *J-V* characteristics of PIPCP:$PC_{61}BM$ devices made with the various contacts are shown in **Figure S1**, in the Supporting Information. The *FF* in PIPCP:$PC_{61}BM$ does not seem to be limited due to contact barriers, though dark carriers diffusing from the contacts may have an effect on the performance, as will be discussed below in the section about non-geminate recombination.

2.2. The Mixed Morphology of PIPCP:$PC_{61}BM$

Achieving an optimal BHJ morphology is critical for high device performance. For this reason, we begin with a characterization of the morphology in PIPCP:$PC_{61}BM$. Specifically, we sought to understand the mixing between PIPCP and $PC_{61}BM$ BHJ films. The morphology of PIPCP:$PC_{61}BM$ was investigated using resonant soft x-ray scattering (RSoXS) and photoconductive atomic force

microscopy (pc-AFM). Soft x-rays used in RSoXS are particularly well-suited for investigating organic blends owing to the strong absorption of elements such as C, N, etc., which are prevalent in organic semiconductors.[18,29,30] In pc-AFM, the surface morphology is imaged using contact-mode AFM, collecting simultaneously a topographic image and a photocurrent image of the same area. The photocurrent is collected by illuminating the sample with white light, and applying a small bias to the sample to induce an electric field in the device. This technique has been used to probe donor and acceptor phases in BHJ films, determined by the sign of the current collected with the pc-AFM tip.[31–35]

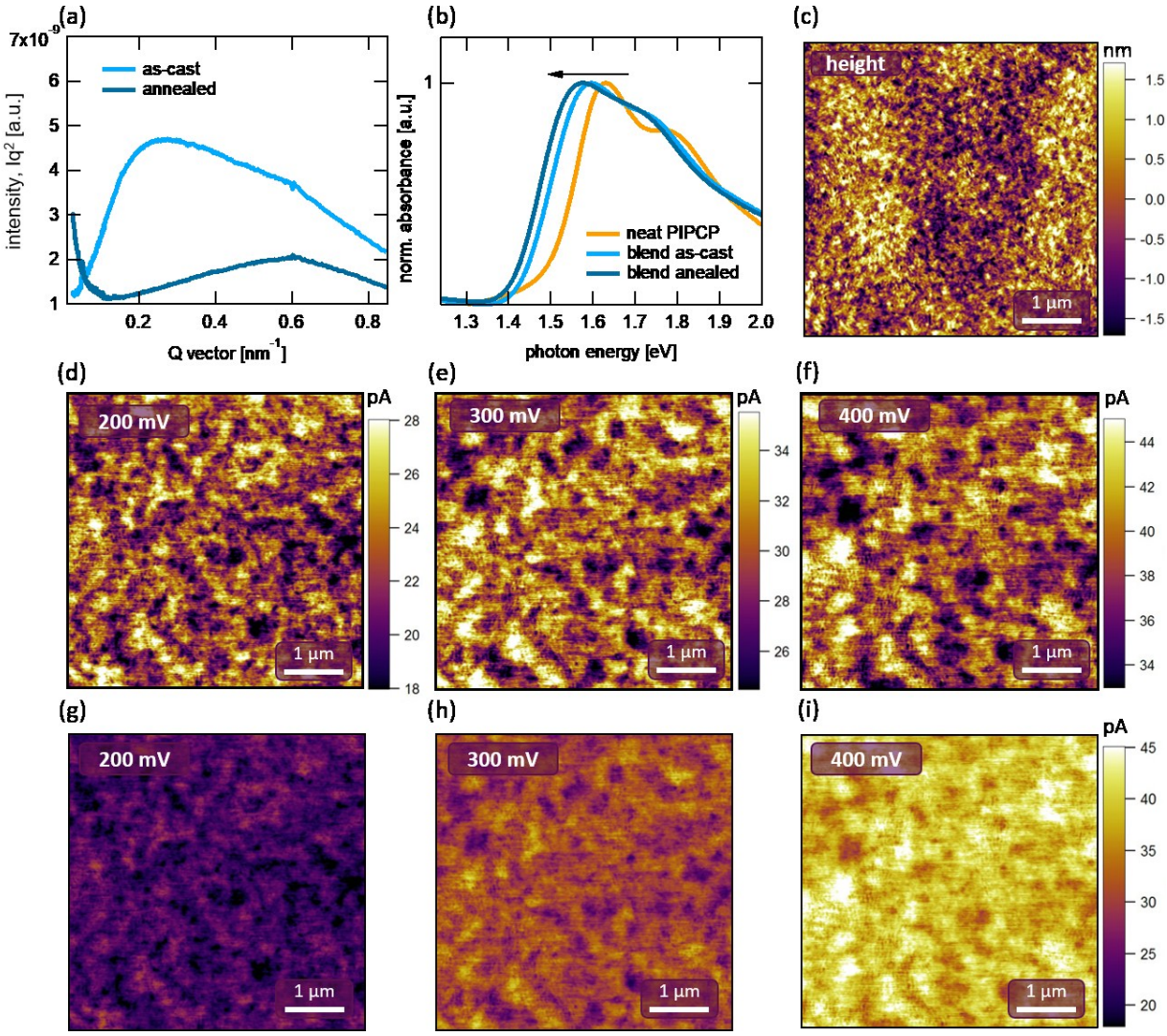

Figure 2. Morphological characterization. (a) RSoXS profile of PIPCP:PC_{61}BM BHJ blends, pristine and annealed at 200 °C. The profiles were Lorentz corrected, and normalized for absorption and film thickness. (b) Film UV-vis absorption spectra of neat PIPCP, pristine PIPCP:PC_{61}BM blend, and PIPCP:PC_{61}BM blend annealed at 200 °C for 10 minutes. (c) Contact-mode topography AFM image for a pristine PIPCP:PC_{61}BM blend film. (d-f) Photocurrent images collected under voltages of (d) 200 mV, (e) 300 mV, and (f) 400 mV applied to the substrate (ITO/ZnO). (g-i) same as images (d-f), redrawn with a normalized current scale, to the right of (i).

Figure 2a shows Lorentz-corrected and circularly-averaged RSoXS profiles of PIPCP:$PC_{61}BM$ blend films as-cast (the condition relevant for the best performing solar cells), and annealed at 200 °C for 10 minutes (annealing was meant to induce different degrees of phase separation). The domain spacing is extracted as the characteristic length, calculated using $d=2\pi/q_{peak}$, where q_{peak} is the peak location, *i.e.* mode, of the scattering intensity. An apparent peak located at $q\approx0.2$ nm^{-1} observed from the as-cast blend indicates a characteristic length of 30 nm in the as-cast thin film. Upon annealing the films at 200 °C for 10 minutes, the peak disappears, indicating the absence of phase separation. This suggests that PIPCP and $PC_{61}BM$ are highly miscible, and given thermal energy they form an intimately mixed morphology instead of relatively pure, separate phases. This is unlike what has been observed for many other polymer:fullerene blend systems.[30,34,35] Furthermore, χ calculations for PIPCP and $PC_{61}BM$ also indicate that the two materials have a high propensity to mix, with a χ of about 0.54, below the critical χ for this system. These calculations are based on the Hansen solubility parameters of the functional groups in PIPCP and $PC_{61}BM$,[36] using the additive functional group method (more information on this is available in the Supporting Information). Although the reliability of χ values derived from Hanson solubility parameters to predict device performance remains uncertain,[37] the low χ value here is in stark contrast to that of a recent high-performance system.[38]

Upon blending PIPCP with $PC_{61}BM$, the low-energy absorption edge red-shifts, corresponding to a reduction in the bandgap of PIPCP (**Figure 2b**). A decrease in the bandgap of PIPCP may be the result of increased conjugation in PIPCP with planarization of the backbone[39,40] but the reason for backbone planarization upon mixing is not currently understood. A red-shift in absorption upon mixing is in contrast to what is generally observed for polymers: more often, PCBM disrupts polymer interchain packing, and may even decrease the effective polymer conjugation. Nonetheless, the red-shift increases upon thermal annealing, and the RSoXS data show that mixing between PIPCP and $PC_{61}BM$ also increases. The red-shift in absorption may therefore be an indication of mixing between PIPCP and $PC_{61}BM$. It is worth noting that while PIPCP and $PC_{61}BM$ are highly miscible and can be driven to a fully mixed morphology, PIPCP retains very high energetic order. This is illustrated by an Urbach energy of ≈27 meV for neat PIPCP, the pristine BHJ, and the annealed BHJ (**Figure S2a**). However, the annealed film has lower *FF* and J_{SC} compared to the as-cast BHJ blend (**Figure S2b**). Within this context, it is interesting to consider the recent study by Venkateshvaran *et al.*[41] on an

IDTBT-based polymer, which showed nearly disorder-free transport, which is thought to arise from the unique tendency of the polymer backbone to remain planar.

Further evidence for the mixed morphology of PIPCP:$PC_{61}BM$ was sought by using pc-AFM (**Figure 2c-i**). **Figure 2c** shows a representative height image of a PIPCP:$PC_{61}BM$ film; **Figure 2d-f** show the photocurrent scans of the same area, with increasing extraction bias. Under the chosen experimental conditions, the pc-AFM Cr/Pt tip is expected to collect holes, which transport through PIPCP domains. As the extraction bias is increased, the current over the entire imaged-area increases, instead of only increasing from certain regions that would then be identified as PIPCP domains. This is in contrast to what has been seen with pc-AFM in other systems that have well-defined phase separation.[31–33] These data illustrate that holes can be extracted from the entire imaged-area, thus giving no indication of clear phase separation between PIPCP and $PC_{61}BM$. In other words, PIPCP domains in the blend are smaller than the resolution of the pc-AFM, and distributed throughout the imaged area. Overall, the RSoXS, red-shifted absorption, and the pc-AFM data suggest that while the as-cast PIPCP:$PC_{61}BM$ film has some separate donor and acceptor domains (also supported by transmission electron microscope images[6]), the film is significantly composed of intimately-mixed regions. An intimately mixed BHJ morphology is expected to cause recombination losses, as was shown even in systems that have sufficient energetic driving force for charge generation.[11,29] Below we investigate the recombination losses in PIPCP:$PC_{61}BM$ and determine the impact of the low-energetic offset and the effect of the high miscibility between PIPCP and $PC_{61}BM$.

2.3. No Field-Dependence of Charge Generation

The poor *FF* of PIPCP:$PC_{61}BM$ BHJ solar cells may be caused by field-dependent splitting of the CT states into free charges, in competition with geminate recombination. Geminate recombination is defined as relaxation of bound hole-electron pairs, which originate from the same photon absorption (schematically represented in **Figure 1c**).

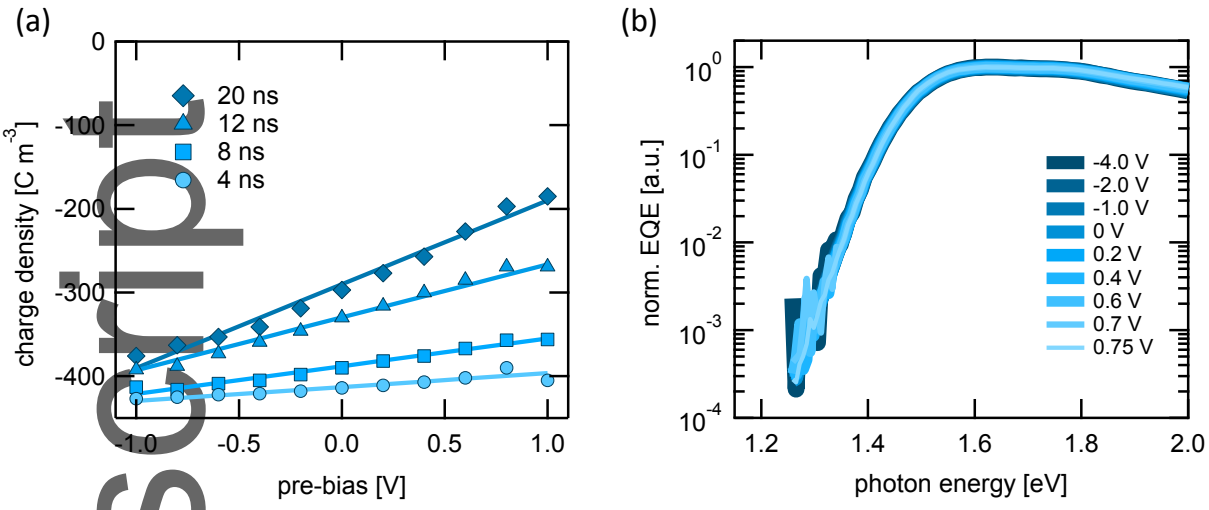

Figure 3. Field-dependence of photocurrent. (a) TDCF data for as-cast PIPCP:$PC_{61}BM$ at different delay times. (b) Normalized bias-dependent EQE at low photon energies, for full spectra refer to the Supporting Information, **Figure S4**.

To determine whether PIPCP:$PC_{61}BM$ blends suffer from field-dependent generation, we referred to time-delayed collection-field (TDCF) measurements. In TDCF measurements the solar cell is held at a particular bias (called the pre-bias) while excitons are generated with a laser pulse. After a specified delay-time, a strong-reverse bias is applied in order to quickly collect all extractable charges that remain. With a time delay that is short enough, such that no charges have recombined before the collection voltage is applied, TDCF can be used to measure the field dependence of charge generation.[11,42]

Figure 3a shows the TDCF results for PIPCP:$PC_{61}BM$, excited at 532 nm, for delay times varying from 20 ns down to 4 ns, and across a range of pre-bias conditions. With a delay of 20 ns between excitation and extraction, one observes a very strong dependence of extracted charge on the pre-bias. The steep dependence might suggest that the generation of charges is indeed field-dependent. However, as the excitation intensity is reduced, the field-dependence of charges collected at a 20 ns delay time is also reduced (**Figure S3**), indicating of non-geminate recombination causing the field-dependent. Furthermore, as the delay time is

shortened, the dependence on the pre-bias decreases, until at a delay of 4 ns (at the limit of the instrument capability), the charge collection shows only a weak dependence on the pre-bias. These results illustrate two findings. First, the strong field dependence seen at 20 ns suggests exceptionally fast non-geminate recombination. At low fields, that is at a pre-bias close to V_{OC}, one can see that after 20 ns nearly half of the charge has already recombined. Second, the TDCF results at a delay of 4 ns suggest that in fact, generation of free charge carriers occurs equally efficiently at all fields. In other words, PIPCP:$PC_{61}BM$ blends do not suffer from strong field-dependent charge generation, but photogenerated charges rapidly undergo recombination.

Despite the absence of field-dependent generation, the photocurrent (dark current subtracted from current under illumination) of PIPCP:$PC_{61}BM$ continues to climb, even up to an effective bias (applied voltage subtracted by the built-in voltage) of 10 V, where the photocurrent is nearly 20 mA/cm^2 (**Figure S4a**). Bias-dependent EQE spectra show that the entire absorption spectrum is field-dependent, though it is more pronounced in the range where PCBM primarily absorbs (**Figure 3b** and **Figure S4**). On the other hand, there is virtually no effect of the photon energy on the bias-dependence of the EQE at energies corresponding to the CT state or low-energy PIPCP absorption (**Figure 3b**). This behavior is opposite to observations using EQE analysis for other low-bandgap polymer systems, where excitation energy was suggested to play a significant role in dissociating excitons generated on the polymer.[43] Therefore, we conclude that the field-dependence in PIPCP:$PC_{61}BM$ does not originate from "hot-exciton" effects, where the excess excitation energy has been suggested to assist in charge generation.

2.4. Temperature-Dependent Photocurrent

Having established that charge generation in PIPCP:$PC_{61}BM$ is not limited by field-dependent generation, despite the very low energetic offset, we investigated the role of temperature on photocurrent generation.

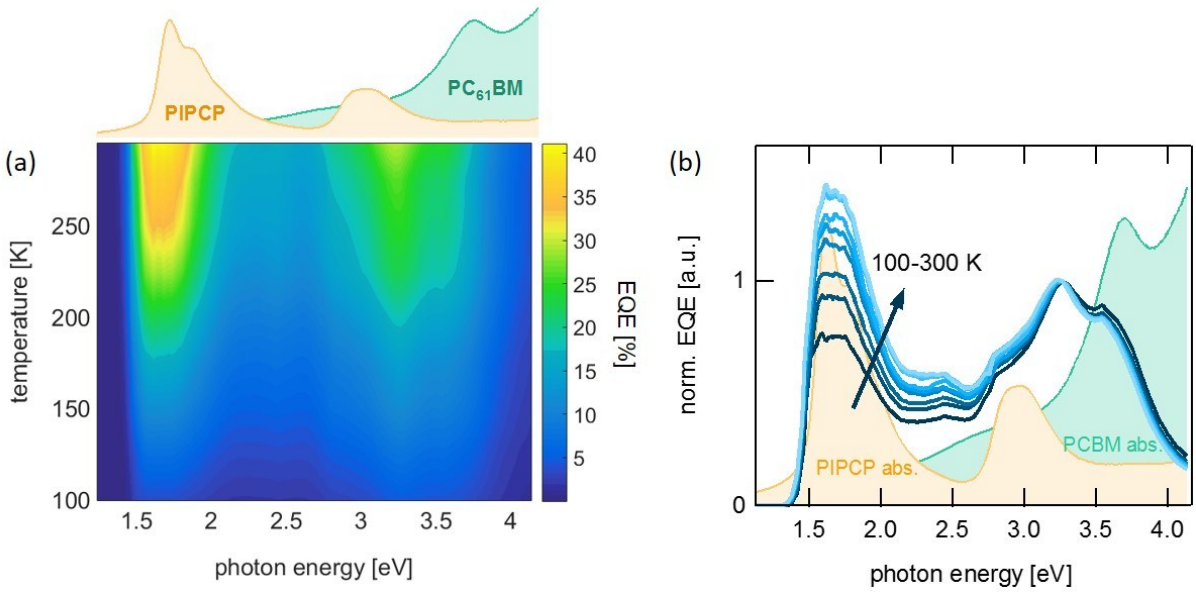

Figure 4. Temperature-dependent photocurrent. Temperature-dependent EQE plotted on (a) a heat map, with the spectral shapes of neat PIPCP and $PC_{61}BM$ absorption above the heat map. (b) The same EQE curves normalized to the EQE at 3.3 eV. Unitless absorption spectra of PIPCP and $PC_{61}BM$ are shown in the background for reference.

Figure 4 shows EQE spectra of PIPCP:$PC_{61}BM$ collected at temperatures ranging from 100-300 K. The heat map in **Figure 4a** shows the evolution of the contributions of higher energy excitations ($PC_{61}BM$ absorption) and lower energy excitations (PIPCP absorption) to the EQE as temperature is reduced. For reference, the absorption spectra of PIPCP and $PC_{61}BM$ is shown above the heat map, at the corresponding photon energies. At room temperature, the EQE is highest for low-photon energy excitations (around 1.6 eV) with another prominent peak at around 3.3 eV. However, as is shown in **Figure 4a**, the temperature-dependence of the EQE spectra also has a clear dependence on excitation-energy. **Figure 4b** shows the same EQE spectra normalized to the EQE at 3.3 eV, and **Figure S5** shows the low-energy region of the EQE. Interestingly, the EQE spectra show that

photocurrent from excitations at energies associated with PIPCP is more temperature-dependent than photocurrent from excitation at energies corresponding to $PC_{61}BM$ absorption. To illustrate the anisotropy, using a simple Arrhenius relationship, it is possible to extract an activation energy for charge generation from temperature-dependent EQE, as was recently demonstrated by Gao *et al.*[44] The activation energies for charge generation from PIPCP excitations (1.5-2.7 eV) and $PC_{61}BM$ excitations (2.7-4.0 eV) come out to be 32 meV and 24 meV, respectively. We assign this to the activation energy of charge generation, because we expect that as soon as charge transfer occurs and free charges are generated, there should be no dependence on the initial energy of excitation. Therefore, the anisotropic temperature dependence should indicate the presence of a barrier for charge generation that is larger for low photon energy excitations than higher-energy excitations.

The spectral temperature dependence of the EQE suggests that excitons originated on PIPCP may separate less efficiently, and are more dependent on thermal activation to escape recombination. Here we recall that mixing between PIPCP and $PC_{61}BM$ reduces the bandgap of PIPCP (absorption data in **Figure 2b**), deepens the ionization potential (IP) of PIPCP, and in so doing also deepens the electron affinity (EA) of PIPCP.[6] Together, these two effects create an energetic landscape that is different from the picture often used to describe the benefits to the mixed phase between pure phases, according to which the mixed phase creates an energetic cascade that may obstruct recombination.[45] One possibility is that the deepening of the EA of PIPCP creates PIPCP states with an EA that is even deeper than $PC_{61}BM$, thereby creating shallow trap-states. Indeed, time-dependent density functional theory (TD-DFT) calculations on the PIPCP Frenkel exciton and the CT state at the interface with $PC_{61}BM$, show that for certain PIPCP/$PC_{61}BM$ molecular configurations the E_{CT} is higher in energy than the PIPCP S_1.[24] Thermal energy at room-temperature may be sufficient for most excitons to escape the shallow traps, but as thermal energy is reduced the energetic landscape increasingly impedes charge generation.

The temperature dependence of the EQE spectra may also be interpreted as resulting from "hot-generation," where electronic excess energy from exciting to $S_{n>1}$ can assist in charge generation.[43] Importantly, however, charge generation in PIPCP:$PC_{61}BM$ is not field-dependent (**Figure 3a**), and the field-dependence of the photocurrent which is observed in the EQE spectra does not appear to

depend on excitation wavelength, until excitation energies where the fullerene may be directly excited[46] (**Figure 3b**, **Figure S4b,c**). Excess electronic energy may assist in charge generation by overcoming energetic barriers in a similar fashion to thermal energy, and its contribution becomes more evident as thermal energy is reduced. These data indicate that field-dependence and temperature-dependence of the EQE have different origins and may thus describe different processes.

2.5. Non-Geminate Recombination

The data presented so far suggest that PIPCP:$PC_{61}BM$ blends do not suffer from field-dependent generation. However, the data are indicative of field-dependent recombination losses. In particular, that the results in **Figure 3a** indicate very fast non-geminate recombination, prompted us to investigate if we can increase the *FF* of PIPCP:$PC_{61}BM$ by improving charge extraction or by reducing the probability of charge encounter and the consequent bimolecular recombination.

Bimolecular recombination occurs as free electrons (holes) travel through the film and encounter holes (electrons) generated from another photon, form a CT state, and recombine, as is illustrated in **Figure 1d**. Since bimolecular recombination is a second-order process, its effect on solar cell performance may depend on factors such as charge-carrier density (bimolecular recombination depends on the product between the hole and electron charge-carrier densities) film thickness (will influence charge-carrier extraction times), and mobility (will dictate how fast charge-carriers encounter each other as well as how fast they can be extracted from the film).

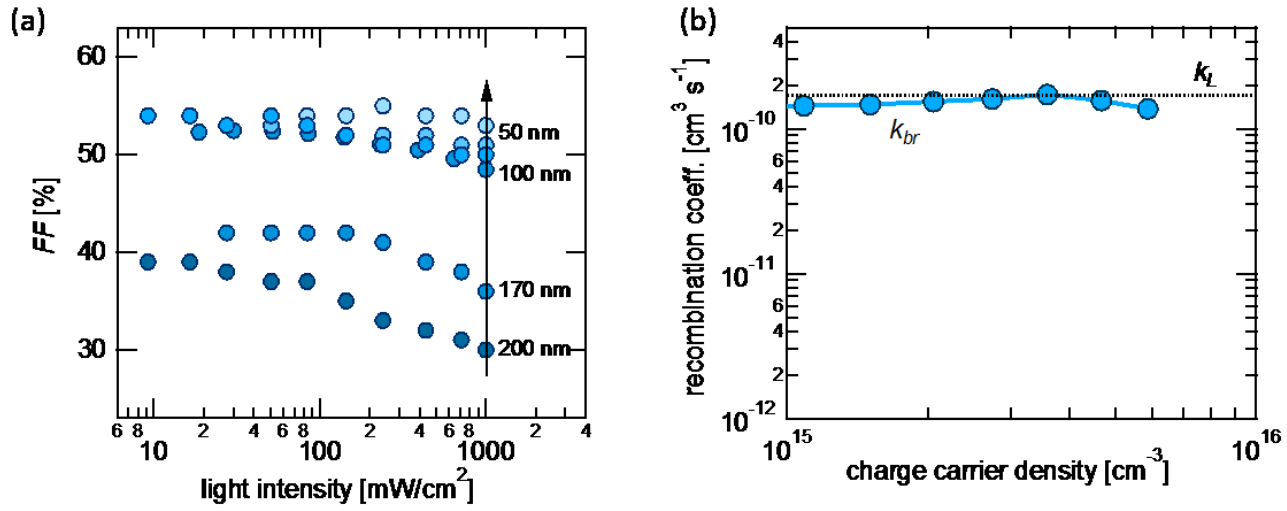

Figure 5. Charge carrier density dependence and thickness-dependence of the *FF*, and the bimolecular recombination coefficient. (a) Light intensity-dependent *FF* values for PIPCP:$PC_{61}BM$ devices with varying active layer thicknesses. (b) Recombination coefficient, k_{rec}, of PIPCP:$PC_{61}BM$ solar cells, for a range of charge carrier densities. The Langevin recombination coefficient, k_L, calculated using the hole and electron mobilities from values shown in **Figure S7**, is shown for reference as a dotted line.

Figure 5 shows the rate coefficient for bimolecular recombination, k_{rec}, for PIPCP:$PC_{61}BM$, and the effects of charge-carrier density and film thickness on the *FF* in PIPCP:$PC_{61}BM$ solar cells. The bimolecular recombination rate, *R*, is described as the product between a recombination coefficient (k_{rec}), the hole (*p*) and electron (*n*) charge-carrier densities, as shown in **Equation 1**:

$$R = \frac{dn}{dt} = k_{rec} np \qquad (1)$$

Light intensity can be used to modulate charge-carrier density in organic solar cells, and in cases where the *FF* is limited by bimolecular recombination, the *FF* has been shown to increase as light-intensity (and by that, charge-carrier density) decreased.[11,47,48] Similarly, thick BHJ films often suffer from low *FF* values due to an increase in extraction times.[49,50] The *FF* of thick PIPCP:$PC_{61}BM$ devices is indeed significantly reduced, most likely due to an increase in bimolecular recombination (**Figure 5a**). As light intensity is reduced, the *FF* of the thick devices increases, though the increase is modest

(10% increase in *FF* with two orders of magnitude decrease in light intensity). The *FF* of the thin devices appears nearly independent of light intensity, reaching a plateau near 56%. It should be noted here that **Figure 5a** only shows data for conditions where dark leakage current (resulting from low shunt resistance) did not influence device performance. If a solar cell device has poor diode characteristics (low shunt resistance), leakage current may distort device performance, especially at low light intensities.[51]

Bimolecular recombination in solar cells can be probed by kinetics of V_{OC} decay. In these measurements, the photovoltage generated by the solar cell is recorded as illumination is turned-off. Because the devices are kept under open-circuit conditions, any changes in the photovoltage must be due to recombination losses and the consequent reduction in quasi Fermi level splitting. Using impedance analysis, we can extract the relationship between charge-carrier density and the corresponding photovoltage.[52–54] Finally, provided with the dynamics of charge-carrier density decay in the solar cell, we derive the recombination rate coefficient, k_{rec}, using **Equation 1**. More detail on this method is available in the experimental section and the Supporting Information.

Our measurements indicate that the charge-carrier density in PIPCP:$PC_{61}BM$ under 1-sun illumination and at V_{OC} conditions is 9×10^{15} cm^{-3} (**Figure S6**), compared to $\approx5\times10^{16}$ cm^{-3} measured in other systems.[54,55] The reason for this low carrier density may lie in the high k_{rec} measured for PIPCP:$PC_{61}B$, k_{rec} is 1.6×10^{-10} cm^{-3} s^{-1} at 1 sun, with very little dependence on charge-carrier density (**Figure 5b**). This recombination coefficient is very high: most organic solar cell blends have k_{rec} values that range between 1×10^{-12} and 1×10^{-10} cm^{-3} s^{-1}.[12,49] To put the k_{rec} value in context, it is often compared to the recombination coefficient as predicted by the Langevin model, k_L, given by **Equation 2**, below:

$$k_L = \frac{q}{\varepsilon\varepsilon_0}(\mu_n + \mu_p) \qquad (2)$$

Here, q- elementary charge; ϵ, ϵ_0 – relative, and vacuum permittivity, respectively; μ_n, μ_p- electron and hole mobilities, respectively. The Langevin model can be taken as the upper limit of recombination in solar cells, as it describes that recombination occurs instantly upon encounter of opposite charges, and is limited only by the rate of encounter. Deviations from the Langevin model

have been used as evidence for an equilibrium between CT states and free charge carriers, where charges form CT states and dissociate many times before they are finally extracted or lost to recombination.[56,57] Furthermore, the Langevin model was originally derived to describe recombination in a single-phase system, and deviations from the Langevin rate coefficient are sometimes attributed to the presence of separate phases for hole and electron transport in BHJ solar cells.[58,59]

Electron and hole mobilities of PIPCP:$PC_{61}BM$ blends, extracted from hole- and electron-only diodes using the space-charge limited current (SCLC) model, are balanced but modest, at 1×10^{-4} cm^2 V^{-1} s^{-1} (**Figure S7**). Using the pristine blend SCLC mobilities and a dielectric constant of 2.95, obtained for this blend using the capacitance spectra (**Figure S6b**), we calculate a k_L of 1.7×10^{-10} cm^{-3} s^{-1}, shown as a dotted line across all charge-carrier densities in **Figure 5b**. In this system k_{rec} and k_L are in very close agreement, yielding a reduction factor (defined as k_{rec}/k_L), of over 0.9. The agreement between k_{rec} and k_L implies that recombination in PIPCP:$PC_{61}BM$ is closely described by the Langevin model. Given that charge generation from primary CT states is efficient, it might then be expected that re-dissociation of nongeminate CT states would also be efficient. However, due to spin statistics, nongeminate CT states will mostly be in a triplet spin state. Recent results by Menke *et al.* indicate that triplet CT states in PIPCP:$PC_{61}BM$ decay very quickly to triplet states in PIPCP, much faster than singlet CT states decay to the ground state.[24] This blend exhibits a relatively unique situation in which charge generation is very efficient, but the bimolecular recombination rate is closely described by the Langevin limit.

The low charge-carrier density may explain the plateau of the *FF* in thin devices at low light-intensities (**Figure 5a**). As the photogenerated charge-carrier density decreases, the presence of dark carriers that diffuse from the contacts[60] becomes increasingly influential. At low photogenerated charge-carrier densities, recombination has been shown to be dominated by non-uniform charge-carrier densities, which results in recombination of majority charge-carriers with minority charge-carriers near the contacts, which is a first-order process.[12,61]

Although the rate of recombination may be large in PIPCP:$PC_{61}BM$, if the rate of charge extraction is significantly faster, then all solar cell parameters (J_{SC}, V_{OC}, and the *FF*) can still be high. When

charge recombination and extraction are in competition, it is possible to tilt the balance towards extraction by increasing the charge-carrier mobilities of the blend. In fact, it has been established in the literature that low charge carrier mobilities will increase charge recombination and the field-dependence of extraction, and thereby reduce the *FF*.[15,27,49,62,63] Analysis of the recombination and extraction lifetimes in PIPCP:$PC_{61}BM$, based on the V_{OC} decay kinetics, shows that under 1 sun illumination, the charge recombination lifetime (2×10^{-6} s) is very close to the charge extraction lifetime (9×10^{-7} s), see the Supporting Information for the equations. To illustrate the meaning of these lifetimes, Bartesaghi *et al*. recently demonstrated a dependence between the *FF* of many experimental and simulated devices and a dimensionless parameter, Θ, which describes the ratio between the recombination lifetime and extraction lifetime.[12] In PIPCP:$PC_{61}BM$, Θ is 6.7×10^{-1}, while to ensure high *FF* values Θ should be on the order of 10^{-3} or smaller.

2.6. Bilayer Solar-Cells Achieve High *FF*

Highly mixed morphologies have been shown to be detrimental to device performance, and the importance of pure domains has been demonstrated in a number of systems.[29,30,64,65] Therefore, in an attempt to decouple effects of energetics and morphology, we fabricated bilayer solar cells by spin-coating a PIPCP layer topped with thermally evaporated C_{60}. We chose to use C_{60} here due to the great molecular similarity between $PC_{61}BM$ and C_{60}, and the ability to thermally evaporate C_{60} and thus maximize phase separation between PIPCP and the fullerene acceptor. Before contact deposition, some PIPCP/C_{60} bilayers were thermally annealed at varying temperatures for 5 minutes in order to induce mixing at the donor/acceptor interface.[66] Pristine bilayers of PIPCP/C_{60}, where phase separation is maximized, indeed achieve a very high *FF* of 72% (**Figure 6a**). Upon thermal annealing, however, the *FF* of the bilayers decreases down to 56%, on par with PIPCP:$PC_{61}BM$ BHJs.

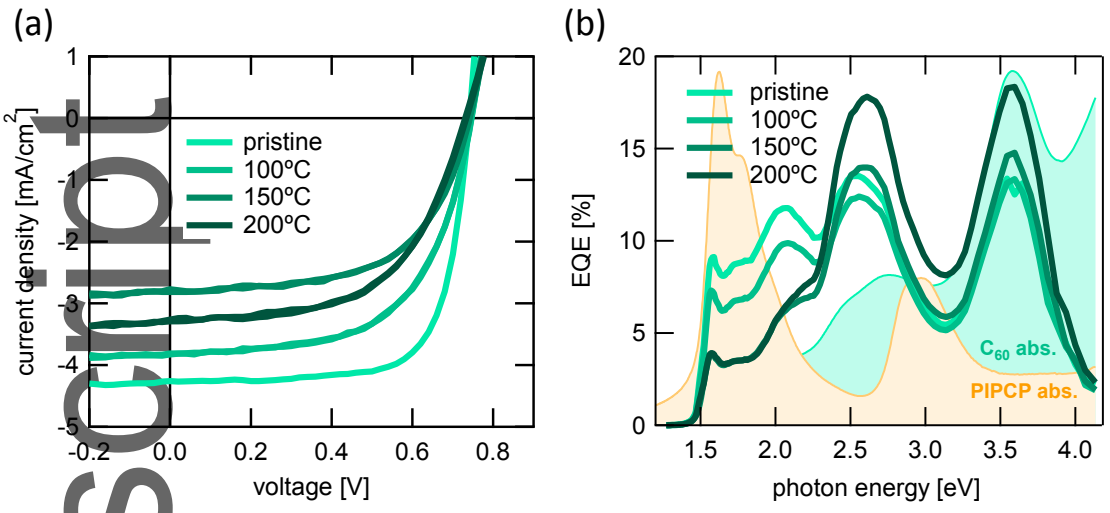

Figure 6. PIPCP/C_{60} bilayer solar cells. (a) 1-sun illuminated *J-V* curves and (b) EQE spectra of pristine PIPCP/C_{60} bilayers, and bilayers annealed at increasingly high temperatures. Unitless absorption spectra of PIPCP and C_{60} are shown in the background for reference.

It should be noted here the LUMO level of C_{60} is deeper than that of $PC_{61}BM$, and thus it is reasonable to expect that the LUMO-LUMO offset between PIPCP/C_{60} is greater than between PIPCP/$PC_{61}BM$. This may explain the lower V_{OC} in the bilayer devices, 0.76 V, and the greater $E_g - qV_{OC}$ = 0.71 eV. Therefore, we wish to focus on the effect of increasing the degree of mixing as the bilayers are annealed, as a parallel to the effect of the high miscibility between PIPCP and $PC_{61}BM$. Mixing at the bilayer interface is expected to increase the J_{SC} due to the increase in surface area for charge generation.[67,68] Interestingly, in the case of PIPCP/C_{60}, the J_{SC} in fact decreases with thermal annealing. EQE spectra of the bilayers (**Figure 6b**) show that the decrease in J_{SC} from pristine bilayers to bilayers annealed at 100 °C, is due to a reduction in current generation from PIPCP absorption (1.5-2.7 eV), while generation from primarily C_{60} absorption (2.7-4.0 eV) remains unchanged. Upon annealing at 150 °C, current generation from PIPCP absorption further decreases, while generation from C_{60} begins to increase, perhaps due to increased order in the C_{60} layer and improved exciton harvesting. Overall, the mixing of PIPCP with C_{60} results in high recombination losses, specifically for excitons generated on PIPCP. This trend in the EQE bears resemblance to the temperature-dependent EQE (**Figure 4**), suggesting that upon mixing, harvesting charges from excitons on PIPCP is

more difficult than excitons generated on $PC_{61}BM$. The decrease in the *FF* of the annealed bilayer devices, however, also suggests that the field-dependence of charge extraction increases with increased mixing between PIPCP and C_{60}, despite the greater energetic offset. These results indicate that intimate mixing in the mixed-phase regions of PIPCP:$PC_{61}BM$ may be the primary reason for the low *FF* in the BHJ devices.

3. Conclusions

With the information discussed in Figures 2-5, we now present a more pertinent schematic representation depicting the recombination, morphology, and energetic landscape in PIPCP:$PC_{61}BM$ (**Figure 7**). The low energetic offset between PIPCP and $PC_{61}BM$ and the intimate mixing do not result in field-dependent charge generation. Instead, the field-dependence limiting the *FF* stems from very fast non-geminate recombination that is competing with charge extraction. Within the view of a balance between charge recombination and charge extraction, in the absence of a field (at V_{OC} conditions) charge recombination dominates (**Figure 7a**). As the field increases, the balance shifts towards charge collection (**Figure 7b**). In addition, because ΔEA of PIPCP and $PC_{61}BM$ is so low, this condition may lead to the formation of shallow exciton traps that require the assistance of thermal energy or excess electronic energy to escape. The possibility for exciton traps was illustrated also by TD-DFT calculations.[24]

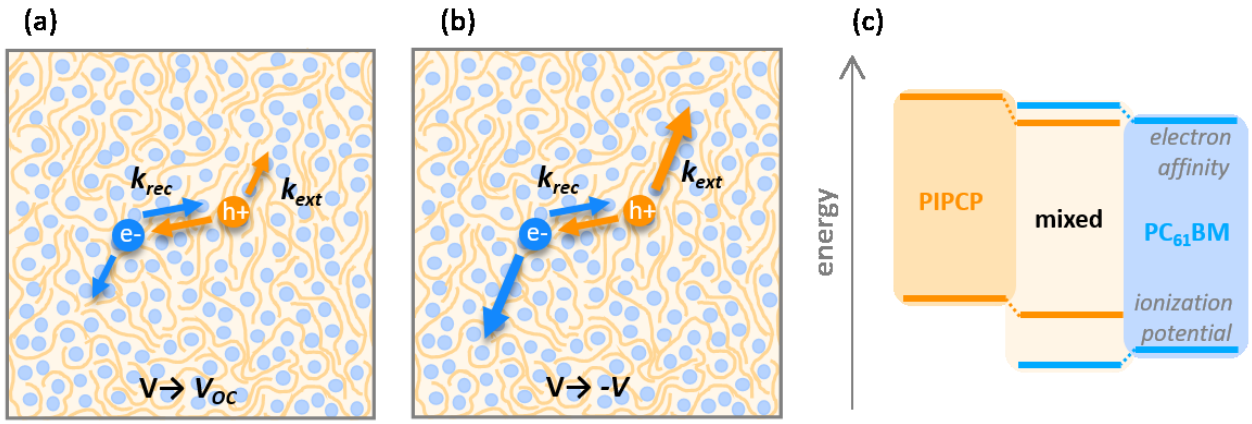

Figure 7. Updated illustration of the morphology, energetics, and the relevant field-dependent recombination losses in PIPCP:$PC_{61}BM$. Charge separation and recombination illustrated as competing processes under varying electric fields: (a) under no internal field (near V_{OC}), (b) at fields that promote charge extraction (reverse bias). k_{rec} and k_{ext} in this figure represent the recombination rate coefficient and extraction rate coefficient, respectively. (c) suggested energetic landscape of a primarily mixed PIPCP:$PC_{61}BM$ film.

Slowing down charge recombination in PIPCP:$PC_{61}BM$ is paramount to improving efficiency. Menke *et al.* estimate that as much as 90% of all recombination events in PIPCP:$PC_{61}BM$ occur via triplet decay pathways.[24] There is evidence in the literature that charge delocalization, achieved by fullerene aggregates, significantly reduces triplet recombination losses, shown by transient absorption.[69,70] In fact, there is a growing body of work emphasizing the importance of aggregation and charge delocalization,[69–79] and the necessity for high purity in the separate donor/acceptor domains.[29,30,64,65] Thus it may be that in order to slow down non-geminate recombination it is necessary to induce pure, separate PIPCP and $PC_{61}BM$ domains (to enhance charge delocalization and escape from the triplet states), without mixed phases (where electron traps may lower photocurrent generation efficiency). Indeed, bilayers fabricated from PIPCP/C_{60} achieve a very high *FF*=72%.

PIPCP holds promise for understanding the fundamentals of charge generation and recombination, given that it retains excellent energetic order in the solid state even when intimately mixed with $PC_{61}BM$. PIPCP:$PC_{61}BM$ can generate up to 14 mA/cm^2 under unfavorable conditions of a highly mixed morphology and little energetic driving force for charge generation, with a high V_{OC} of 0.90 V. A number of studies have been drawing attention to results which indicate that efficient charge generation and collection can be achieved also with minimal energetic offsets.[75,80] While some highlight the importance of highly ordered donor and acceptor domains and high dielectric constants,[80] others focus on an entropic driving force for charge generation.[75] If it were possible to fabricate a BHJ with pure PIPCP and $PC_{61}BM$ phases, there is good reason to believe that the *FF* and the J_{SC} would increase, leading to a BHJ device with very high performance.

To improve the performance of PIPCP as a donor material in OPV we must therefore find the appropriate methods to control the BHJ morphology. To achieve this, a few routes may be possible: (i) It may be that film-formation techniques which do not rely on the self-assembly of the donor and acceptor materials from a homogeneous solution, such as sequential processing of the donor and acceptor,[81] can achieve improved BHJ morphologies. (ii) PIPCP could be combined with a non-fullerene acceptor such that the two components do not have such a high degree of mixing. (iii) Modifying the solubility of PIPCP by side-chain engineering may afford the use of solvents which are better suited for PIPCP or $PC_{61}BM$, as was demonstrated for a series of semiconductors by Liu *et al.*[18] (iv) It may be possible to vary the morphology and improve the performance of PIPCP:$PC_{61}BM$ by fabricating a ternary blend; very high *FF* values have recently been achieved by fabricating ternary BHJ blends.[17,82] These considerations for morphological control are not specific to PIPCP:$PC_{61}BM$, and should be at the forefront of our attention as we design new materials for efficient OPVs and study device optimization.

4. Experimental Section

Sample preparation. PIPCP was synthesized according to the previously reported scheme.[23] PIPCP:$PC_{61}BM$ solutions were prepared at a ratio of 1:2 w/w, dissolved at 18 mg/mL in 3:2 CF:CB v/v, and spun at 2000 RPM. To achieve devices of varying thicknesses, solution concentration and spin speeds were varied, but solids ratio and solvents ratio were kept constant. BHJ devices were fabricated in inverted structure. The ZnO layer was prepared on ITO sputtered glass substrates according to the sol-gel method, described in a previous publication.[83] BHJ active layers were spin-coated from the blend solution at a spin speed of 1500 RPM. The devices were completed with a thermally deposited MoOx/Ag top-contact. The final BHJ device structure for most measurements reported herein is as follows: ITO/ZnO (40 nm)/PIPCP:$PC_{61}BM$ (100-110 nm)/MoOx (6 nm)/Ag (100 nm).

Bilayer devices were fabricated on ITO sputtered glass substrates, coated with thermally evaporated MoOx (10 nm). PIPCP was dissolved at 6 mg/mL in 3:2 CF:CB v/v, and spin-coated at 2000

RPM, followed by a thermally evaporated C_{60} layer. Annealed bilayer devices were placed directly on a hot plate at the specified temperature for 5 minutes. Devices were completed by evaporating a top contact: bathocuproine (BCP) and Al. The final bilayer device structure is as follows: ITO/MoOx (10 nm)/PIPCP (60 nm)/C_{60} (45 nm)/BCP (5 nm)/Al (100 nm).

Current-voltage characteristics. Solar-cell device properties were measured under illumination by a simulated 100 mW cm^{-2} AM1.5G light source using a 300 W Xe arc lamp with an AM 1.5 global filter. The irradiance was adjusted to 1-sun using a standard silicon photovoltaic cell with a protective KG1 filter calibrated by the National Renewable Energy Laboratory.

External and internal quantum efficiency measurements. EQE characteristics were measured in a nitrogen-filled glovebox using a 75 W Xe light source, monochromator, optical chopper, lock-in amplifier, and a National Institute of Standards and Technology calibrated silicon photodiode for power-density calibration. Bias-dependent EQE was collected on the same setup, coupled to a Keithley source-measure-unit which was used to apply a bias while the EQE spectra were recorded. Temperature-dependent EQE measurements were collected following a similar procedure, using a nitrogen-cooled cryostat.

Total absorption of solar cell devices was measured with a Perkin Elmer integrating sphere, and corrected for parasitic absorption as determined using a transfer matrix model.[84] Subtracting the parasitic absorption from the total device absorption then gives the active layer absorption, and dividing EQE spectra by the corresponding active layer absorption gives the IQE spectra of the device.

Time-Delayed Collection Field measurements. Time-Delayed Collection Field measurements. Excitation is realized by a laser system consisting of an Ekspla NT-242-500 Laser operating at 500 Hz. The beam is attenuated via neutral density filters to a fluence of 0.06 μJ/cm^2. The pre- and collection voltage is applied via an Agilent 81150A pulse generator in combination with a home-built amplifier. Currents through the devices are measured via a 50 Ω resistor and recorded with an Agilent Infiniium DSO9054H oscilloscope.

Electroluminescence. Electroluminescence spectra were collected in air from encapsulated solar cell devices, by applying a bias that is close to the turn-on voltage of the devices. The resulting emission was collected with a CCD Si detector, cooled to -70°C. The spectra were corrected for detector response using a blackbody spectrum.

Single-carrier diodes. Solutions for single-carrier diode measurements were prepared using the same blend ratio and solvent ratio as the solar cell devices, but at a solids concentration of 30 mg/mL. This was done to increase the accuracy of the space-charge limited current analysis, which has a cubed dependence on film thickness. Hole-only diodes were fabricated using the following device structure: ITO/MoOx (10 nm)/PIPCP:PC_{61}BM (300 nm)/MoOx (10 nm)/Ag (100 nm). Electron only diodes had the following device structure: ITO/ZnO (40 nm)/PIPCP:PC_{61}BM (300 nm)/Ca (10 nm)/Al (100 nm). To determine the charge carrier mobility, the *J-V* of the hole- or electron-only devices were measured in the dark. The applied bias was corrected for the built-in voltage, and the current was fit to the SCLC model, $J = \frac{9}{8}\epsilon\epsilon_0\mu\frac{(V-V_{bi})^2}{L^3}$. In this equation, J is the current density, ε is the relative permittivity and ε_0 is the vacuum permittivity, V is the applied voltage and V_{bi} is the built-in voltage, L is device thickness, and μ is the charge-carrier mobility.

Open-circuit voltage decay. Measurements were performed on BHJ devices loaded into a nitrogen filled cryostat. Devices were illuminated with a single, high-power white LED (CREE XT-E W130) controlled by a square wave function generator (Stanford Research Systems) attached to a diode switch. Using a focusing lens, illumination intensity can reach above 1 sun. With an LED turn-off time of 200 ns, the setup has a time resolution of ~500 ns. The device photovoltage was measured using a high-impedance voltage follower and an oscilloscope (Techtronix) set with a 200 ns resolution. The repetition rate of the function generator and was set so that the photovoltage produced by the device reached less than 50 mV after each pulse to prevent the possibility of device charging.

Impedance analysis. Devices were illuminated with an AM1.5 solar simulator (300 W Xe arc lamp with an AM 1.5 global filter) that was attenuated using neutral density filters. The solar simulator irradiance was calibrated using a standard silicon photovoltaic cell with a protective KG1 filter calibrated by the National Renewable Energy Laboratory. Light and dark *J-V* curves were measured

using a source-meter (Keithley 2602), and the device impedance response in the dark and under illumination was measured with an impedance analyzer (Solartron SI 1255, SI 1287) with an AC amplitude of 100 mV.

Resonant soft x-ray scattering. R-SoXS measurements were performed with transmission geometry at beamline 11.0.1.2 at the advanced light source (ALS), Lawrence Berkeley National Laboratory.[85] Samples for R-SoXS measurements were prepared on a PSS coated SiO_2 substrate under the same conditions as those used for device fabrication, and then transferred by floating with water to a 1.5 × 1.5 mm, 100 nm thick Si3N4 membrane supported by a 5 × 5 mm, 200 μm thick Si frame (Norcada Inc.). Two dimensional scattering patterns were collected on an in-vacuum (1×10^{-7} Torr) CCD camera (Princeton Instrument PI-MTE). The beam size at the sample is ~100 μm by 200 μm, which gives good statistics. Owing to a lack of absolute flux normalization, the absolute composition cannot be obtained by only R-SoXS.

Photoconductive atomic force microscopy. pc-AFM measurements were performed with an Asylum Research MFP-3D microscope sitting atop an inverted optical microscope (Olympus, IX71). All measurements were done under inert atmosphere. In this work, the bias was applied to the substrate, and the current was recorded by internal preamplifier (Asylum Research ORCA head model). Chromium/Platinum-coated silicon probes with a spring constant of 0.2 N m^{-1} and resonant frequency of 13 kHz (Budget Sensors) were used. A white light source with a power of 30 W cm^{-2} was used for photocurrent imaging. The light was focused on the sample through an inverted optical microscope (Olympus) and then the tip was positioned at the center of the illumination spot. The illuminated spot size at the sample surface was measured to be approximately 160 μm in diameter.

Supporting Information

Supporting Information is available from the Wiley Online Library or from the author.

Acknowledgements

This collaborative project was supported by the Department of the Navy, Office of Naval Research (Award No. N00014-14-1-0580). DN and JAL gratefully acknowledge the BNBF for funding in the project UNVEIL. The high resolution TDCF setup was funded by the Deutsche Forschungsgesellschaft (INST 336/94-1 FUGG). X.J. and H.A. gratefully acknowledge the support by the Office of Naval Research grant N00141512322. X-ray data acquired at ALS was supported by Department of Energy under the contract No. DE-AC02-05CH11231.

Received: ((will be filled in by the editorial staff))
Revised: ((will be filled in by the editorial staff))
Published online: ((will be filled in by the editorial staff))

References

[1] W. Li, K. H. Hendriks, A. Furlan, M. M. Wienk, R. A. J. Janssen, *J. Am. Chem. Soc.* **2015**, *137*, 2231.

[2] M. A. Faist, T. Kirchartz, W. Gong, R. S. Ashraf, I. McCulloch, J. C. de Mello, N. J. Ekins-Daukes, D. D. C. Bradley, J. Nelson, *J. Am. Chem. Soc.* **2012**, *134*, 685.

[3] J. Liu, S. Chen, D. Qian, B. Gautam, G. Yang, J. Zhao, J. Bergqvist, F. Zhang, W. Ma, H. Ade, O. Inganäs, K. Gundogdu, F. Gao, H. Yan, *Nat. Energy* **2016**, *1*, 16089.

[4] Y. Li, X. Liu, F.-P. Wu, Y. Zhou, Z.-Q. Jiang, B. Song, Y. Xia, Z.-G. Zhang, F. Gao, O. Inganäs, Y. Li, L.-S. Liao, *J. Mater. Chem. A* **2016**, *4*, 5890.

[5] K. Kawashima, Y. Tamai, H. Ohkita, I. Osaka, K. Takimiya, *Nat. Commun.* **2015**, *6*, 10085.

[6] N. A. Ran, J. A. Love, C. J. Takacs, A. Sadhanala, J. K. Beavers, S. D. Collins, Y. Huang, M. Wang, R. H. Friend, G. C. Bazan, T.-Q. Nguyen, *Adv. Mater.* **2015**, 1482.

[7] W. Li, K. H. Hendriks, A. Furlan, M. M. Wienk, R. A. J. Janssen, *J. Am. Chem. Soc.* **2015**, *137*, 2231.

[8] M.-H. Jao, H.-C. Liao, W.-F. Su, *J. Mater. Chem. A* **2016**, *4*, 5784.

[9] G. F. A. Dibb, F. C. Jamieson, A. Maurano, J. Nelson, J. R. Durrant, *J. Phys. Chem. Lett.* **2013**, *4*, 803.

[10] S. Albrecht, J. R. Tumbleston, S. Janietz, I. Dumsch, S. Allard, U. Scherf, H. Ade, D. Neher, *J. Phys. Chem. Lett.* **2014**, *5*, 1131.

[11] C. M. Proctor, S. Albrecht, M. Kuik, D. Neher, T.-Q. Nguyen, *Adv. Energy Mater.* **2014**, 1400230.

[12] D. Bartesaghi, I. del C. Pérez, J. Kniepert, S. Roland, M. Turbiez, D. Neher, L. J. A. Koster, *Nat. Commun.* **2015**, *6*, 7083.

[13] P. Kaienburg, U. Rau, T. Kirchartz, *Phys. Rev. Appl.* **2016**, *6*, 024001.

[14] T. Kirchartz, T. Agostinelli, M. Campoy-Quiles, W. Gong, J. Nelson, *J. Phys. Chem. Lett.* **2012**, *3*, 3470.

[15] D. Neher, J. Kniepert, A. Elimelech, L. J. A. Koster, *Sci. Rep.* **2016**, *6*, 24861.

[16] N. Zhou, X. Guo, R. P. Ortiz, T. Harschneck, E. F. Manley, S. J. Lou, P. E. Hartnett, X. Yu, N. E. Horwitz, P. M. Burrezo, T. J. Aldrich, J. T. López Navarrete, M. R. Wasielewski, L. X. Chen, R. P. H. Chang, A. Facchetti, T. J. Marks, *J. Am. Chem. Soc.* **2015**, *137*, 12565.

[17] N. Gasparini, X. Jiao, T. Heumueller, D. Baran, G. J. Matt, S. Fladischer, E. Spiecker, H. Ade, C. J. Brabec, T. Ameri, *Nat. Energy* **2016**, *1*, 16118.

[18] Y. Liu, J. Zhao, Z. Li, C. Mu, W. Ma, H. Hu, K. Jiang, H. Lin, H. Ade, H. Yan, *Nat. Commun.* **2014**, *5*, 5293.

[19] M. Li, F. Liu, X. Wan, W. Ni, B. Kan, H. Feng, Q. Zhang, X. Yang, Y. Wang, Y. Zhang, Y. Shen, T. P. Russell, Y. Chen, *Adv. Mater.* **2015**, *27*, 6296.

[20] J.-L. Wang, F. Xiao, J. Yan, Z. Wu, K.-K. Liu, Z.-F. Chang, R.-B. Zhang, H. Chen, H.-B. Wu, Y. Cao, *Adv. Funct. Mater.* **2016**, *26*, 1803.

[21] J.-L. Wang, K.-K. Liu, J. Yan, Z. Wu, F. Liu, F. Xiao, Z.-F. Chang, H.-B. Wu, Y. Cao, T. P. Russell, *J. Am. Chem. Soc.* **2016**, *138*, 7687.

[22] K. Sun, Z. Xiao, S. Lu, W. Zajaczkowski, W. Pisula, E. Hanssen, J. M. White, R. M. Williamson, J. Subbiah, J. Ouyang, A. B. Holmes, W. W. H. Wong, D. J. Jones, *Nat. Commun.* **2015**, *6*, 6013.

[23] M. Wang, H. Wang, T. Yokoyama, X. Liu, Y. Huang, Y. Zhang, T.-Q. Nguyen, S. Aramaki, G. C. Bazan, *J. Am. Chem. Soc.* **2014**, *136*, 12576.

[24] S. M. Menke, A. Sadhanala, M. Nikolka, N. A. Ran, M. K. Ravva, S. Abdel-Azeim, H. L. Stern, M. Wang, H. Sirringhaus, T.-Q. Nguyen, J.-L. Brédas, G. C. Bazan, R. H. Friend, *ACS Nano* **2016**, *10*, 10736.

[25] A. Kumar, G. Lakhwani, E. Elmalem, W. T. S. Huck, A. Rao, N. C. Greenham, R. H. Friend, *Energy Environ. Sci.* **2014**, *7*, 2227.

[26] Z.-K. Tan, Y. Vaynzof, D. Credgington, C. Li, M. T. L. Casford, A. Sepe, S. Huettner, M. Nikolka, F. Paulus, L. Yang, H. Sirringhaus, N. C. Greenham, R. H. Friend, *Adv. Funct. Mater.* **2014**, *24*, 3051.

[27] W. Tress, K. Leo, M. Riede, *Phys. Rev. B* **2012**, *85*, 155201.

[28] B. E. Lassiter, G. Wei, S. Wang, J. D. Zimmerman, V. V. Diev, M. E. Thompson, S. R. Forrest, *Appl. Phys. Lett.* **2011**, *98*, 243307.

[29] S. Mukherjee, C. M. Proctor, G. C. Bazan, T.-Q. Nguyen, H. Ade, *Adv. Energy Mater.* **2015**, *5*, 1500877.

[30] B. A. Collins, Z. Li, J. R. Tumbleston, E. Gann, C. R. McNeill, H. Ade, *Adv. Energy Mater.* **2013**, *3*, 65.

[31] M. Guide, X.-D. Dang, T.-Q. Nguyen, *Adv. Mater.* **2011**, *23*, 2313.

[32] X.-D. Dang, A. B. Tamayo, J. Seo, C. V. Hoven, B. Walker, T.-Q. Nguyen, *Adv. Funct. Mater.* **2010**, *20*, 3314.

[33] X.-D. Dang, A. Mikhailovsky, T.-Q. Nguyen, *Appl. Phys. Lett.* **2010**, *97*, 113303.

[34] D. C. Coffey, O. G. Reid, D. B. Rodovsky, G. P. Bartholomew, D. S. Ginger, *Nano Lett.* **2007**, *7*, 738.

[35] C. Groves, O. G. Reid, D. S. Ginger, *Acc. Chem. Res.* **2010**, *43*, 612.

[36] E. M. Pearce, *J. Polym. Sci. Polym. Lett. Ed.* **1977**, *15*, 56.

[37] D. Leman, M. A. Kelly, S. Ness, S. Engmann, A. Herzing, C. Snyder, H. W. Ro, R. J. Kline, D. M. DeLongchamp, L. J. Richter, *Macromolecules* **2015**, *48*, 383.

[38] L. Ye, W. Zhao, S. Li, S. Mukherjee, J. H. Carpenter, O. Awartani, X. Jiao, J. Hou, H. Ade, *Adv. Energy Mater.* **2016**, *6*, 1602000.

[39] R. Hoffmann, C. Janiak, C. Kollmar, *Macromolecules* **1991**, *24*, 3725.

[40] F. Panzer, H. Bässler, A. Köhler, *J. Phys. Chem. Lett.* **2017**, *8*, 114.

[41] D. Venkateshvaran, M. Nikolka, A. Sadhanala, V. Lemaur, M. Zelazny, M. Kepa, M. Hurhangee, A. J. Kronemeijer, V. Pecunia, I. Nasrallah, I. Romanov, K. Broch, I. McCulloch, D. Emin, Y. Olivier, J. Cornil, D. Beljonne, H. Sirringhaus, *Nature* **2014**, *515*, 384.

[42] S. Albrecht, W. Schindler, J. Kurpiers, J. Kniepert, J. C. Blakesley, I. Dumsch, S. Allard, K. Fostiropoulos, U. Scherf, D. Neher, *J. Phys. Chem. Lett.* **2012**, *3*, 640.

[43] T. Hahn, J. Geiger, X. Blase, I. Duchemin, D. Niedzialek, S. Tscheuschner, D. Beljonne, H. Bässler, A. Köhler, *Adv. Funct. Mater.* **2015**, *25*, 1287.

[44] F. Gao, W. Tress, J. Wang, O. Inganäs, *Phys. Rev. Lett.* **2015**, *114*, 128701.

[45] S. Sweetnam, K. R. Graham, G. O. Ngongang Ndjawa, T. Heumüller, J. A. Bartelt, T. M. Burke, W. Li, W. You, A. Amassian, M. D. McGehee, *J. Am. Chem. Soc.* **2014**, *136*, 14078.

[46] T. Hahn, S. Tscheuschner, C. Saller, P. Strohriegl, P. Boregowda, T. Mukhopadhyay, S. Patil, D. Neher, H. Bässler, A. Köhler, *J. Phys. Chem. C* **2016**, *120*, 25083.

[47] L. Wu, H. Zang, Y.-C. Hsiao, X. Zhang, B. Hu, *Appl. Phys. Lett.* **2014**, *104*, 153903.

[48] R. Mauer, I. A. Howard, F. Laquai, *J. Phys. Chem. Lett.* **2010**, *1*, 3500.

[49] J. A. Bartelt, D. Lam, T. M. Burke, S. M. Sweetnam, M. D. McGehee, *Adv. Energy Mater.* **2015**, *5*, 1500577.

[50] M. Lenes, L. J. A. Koster, V. D. Mihailetchi, P. W. M. Blom, *Appl. Phys. Lett.* **2006**, *88*, 243502.

[51] C. M. Proctor, T.-Q. Nguyen, *Appl. Phys. Lett.* **2015**, *106*, 083301.

[52] V. V. Brus, C. M. Proctor, N. A. Ran, T.-Q. Nguyen, *Adv. Energy Mater.* **2016**, *6*, 1502250.

[53] C. M. Proctor, C. Kim, D. Neher, T.-Q. Nguyen, *Adv. Funct. Mater.* **2013**, *23*, 3584.

[54] S. D. Collins, C. M. Proctor, N. A. Ran, T.-Q. Nguyen, *Adv. Energy Mater.* **2015**, 1501721.

[55] I. Lange, J. Kniepert, P. Pingel, I. Dumsch, S. Allard, S. Janietz, U. Scherf, D. Neher, *J. Phys. Chem. Lett.* **2013**, *4*, 3865.

[56] T. M. Burke, S. Sweetnam, K. Vandewal, M. D. McGehee, *Adv. Energy Mater.* **2015**, *5*, 1500123.

[57] A. J. Ferguson, N. Kopidakis, S. E. Shaheen, G. Rumbles, *J. Phys. Chem. C* **2011**, *115*, 23134.

[58] M. C. Heiber, T.-Q. Nguyen, C. Deibel, *Phys. Rev. B* **2016**, *93*, 205204.

[59] M. C. Heiber, C. Baumbach, V. Dyakonov, C. Deibel, *Phys. Rev. Lett.* **2015**, *114*, 136602.

[60] I. Lange, J. C. Blakesley, J. Frisch, A. Vollmer, N. Koch, D. Neher, *Phys. Rev. Lett.* **2011**, *106*, 216402.

[61] F. Deledalle, P. Shakya Tuladhar, J. Nelson, J. R. Durrant, T. Kirchartz, *J. Phys. Chem. C* **2014**, *118*, 8837.

[62] C. M. Proctor, J. A. Love, T.-Q. Nguyen, *Adv. Mater.* **2014**, *26*, 5957.

[63] M. Stolterfoht, A. Armin, B. Philippa, D. Neher, *J. Phys. Chem. Lett.* **2016**, *7*, 4716.

[64] S. V. Kesava, Z. Fei, A. D. Rimshaw, C. Wang, A. Hexemer, J. B. Asbury, M. Heeney, E. D. Gomez, *Adv. Energy Mater.* **2014**, *4*, 1400116.

[65] B. P. Lyons, N. Clarke, C. Groves, *Energy Environ. Sci.* **2012**, *5*, 7657.

[66] N. D. Treat, M. A. Brady, G. Smith, M. F. Toney, E. J. Kramer, C. J. Hawker, M. L. Chabinyc, *Adv. Energy Mater.* **2011**, *1*, 82.

[67] G. O. Ngongang Ndjawa, K. R. Graham, R. Li, S. M. Conron, P. Erwin, K. W. Chou, G. F. Burkhard, K. Zhao, E. T. Hoke, M. E. Thompson, M. D. McGehee, A. Amassian, *Chem. Mater.* **2015**, *27*, 5597.

[68] S. Shoaee, S. Mehraeen, J. G. Labram, J.-L. Brédas, D. D. C. Bradley, V. Coropceanu, T. D. Anthopoulos, J. R. Durrant, *J. Phys. Chem. Lett.* **2014**, *5*, 3669.

[69] A. Rao, P. C. Y. Chow, S. Gélinas, C. W. Schlenker, C.-Z. Li, H.-L. Yip, A. K.-Y. Jen, D. S. Ginger, R. H. Friend, *Nature* **2013**, *500*, 435.

[70] S. Gélinas, A. Rao, A. Kumar, S. L. Smith, A. W. Chin, J. Clark, T. S. van der Poll, G. C. Bazan, R. H. Friend, *Science* **2014**, *343*, 512.

[71] C. Schwarz, H. Bässler, I. Bauer, J.-M. Koenen, E. Preis, U. Scherf, A. Köhler, *Adv. Mater.* **2012**, *24*, 922.

[72] A. A. Bakulin, A. Rao, V. G. Pavelyev, P. H. M. van Loosdrecht, M. S. Pshenichnikov, D. Niedzialek, J. Cornil, D. Beljonne, R. H. Friend, *Science* **2012**, *335*, 1340.

[73] C. Deibel, T. Strobel, V. Dyakonov, *Phys. Rev. Lett.* **2009**, *103*, 036402.

[74] G. D'Avino, L. Muccioli, Y. Olivier, D. Beljonne, *J. Phys. Chem. Lett.* **2016**, *7*, 536.

[75] A. C. Jakowetz, M. L. Böhm, J. Zhang, A. Sadhanala, S. Huettner, A. A. Bakulin, A. Rao, R. H. Friend, *J. Am. Chem. Soc.* **2016**, *138*, 11672.

[76] H. Tamura, I. Burghardt, *J. Am. Chem. Soc.* **2013**, *135*, 16364.

[77] B. Yang, Y. Yi, C.-R. Zhang, S. G. Aziz, V. Coropceanu, J.-L. Bredas, *J. Phys. Chem. C* **2014**, *118*, 27648.

[78] X.-K. Chen, M. K. Ravva, H. Li, S. M. Ryno, J.-L. Brédas, *Adv. Energy Mater.* **2016**, 1601325.

[79] B. Bernardo, D. Cheyns, B. Verreet, R. D. Schaller, B. P. Rand, N. C. Giebink, *Nat. Commun.* **2014**, *5*, 3245.

[80] N. Bansal, L. X. Reynolds, A. MacLachlan, T. Lutz, R. S. Ashraf, W. Zhang, C. B. Nielsen, I. McCulloch, D. G. Rebois, T. Kirchartz, M. S. Hill, K. C. Molloy, J. Nelson, S. A. Haque, *Sci. Rep.* **2013**, *3*, 1531.

[81] J. C. Aguirre, S. A. Hawks, A. S. Ferreira, P. Yee, S. Subramaniyan, S. A. Jenekhe, S. H. Tolbert, B. J. Schwartz, *Adv. Energy Mater.* **2015**, *5*, 1402020.

[82] N. Gasparini, L. Lucera, M. Salvador, M. Prosa, G. D. Spyropoulos, P. Kubis, H.-J. Egelhaaf, C. J. Brabec, T. Ameri, *Energy Environ. Sci.* **2017**, *10*, 885.

[83] Y. Sun, J. H. Seo, C. J. Takacs, J. Seifter, A. J. Heeger, *Adv. Mater.* **2011**, *23*, 1679.

[84] G. F. Burkhard, E. T. Hoke, M. D. McGehee, *Adv. Mater.* **2010**, *22*, 3293.

[85] E. Gann, A. T. Young, B. A. Collins, H. Yan, J. Nasiatka, H. A. Padmore, H. Ade, A. Hexemer, Wang, *Rev. Sci. Instrum.* **2012**, *83*, 045110.

To realize organic solar cells with high open circuit voltages and short circuit currents, it is necessary to minimize the energetic offset between the donor and acceptor materials. Recently, a number of reports have highlighted donor:acceptor blends with low offsets that achieve good photovoltaic performance. However, the *FF* of those solar cells has remained below 60%. This manuscript describes a comprehensive study of the recombination and generation in one such system, PIPCP:$PC_{61}BM$, to determine the cause to the limited *FF*.

Keywords: organic solar cells, recombination, energetic offset, fill factor, morphology

Niva A. Ran, John A. Love, Michael C. Heiber, Xuechen Jiao, Michael P. Hughes, Akchheta Karki, Ming Wang, Viktor V. Brus, Hengbin Wang, Dieter Neher, Harald Ade, Guillermo C. Bazan, Thuc-Quyen Nguyen**

Charge Generation and Recombination in an Organic Solar Cell with Low Energetic Offsets

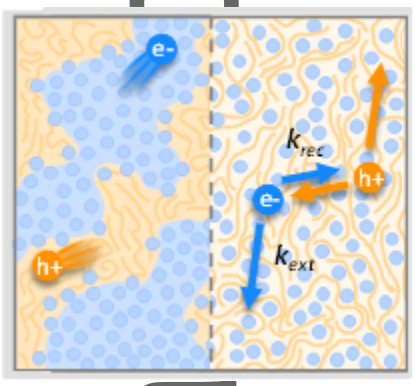

Supporting Information

Charge Generation and Recombination in an Organic Solar Cell with Low Energetic Offsets

Niva A. Ran, John A. Love, Michael C. Heiber, Xuechen Jiao, Michael P. Hughes, Akchheta Karki, Ming Wang, Viktor V. Brus, Hengbin Wang, Dieter Neher, Harald Ade, Guillermo C. Bazan, Thuc-Quyen Nguyen**

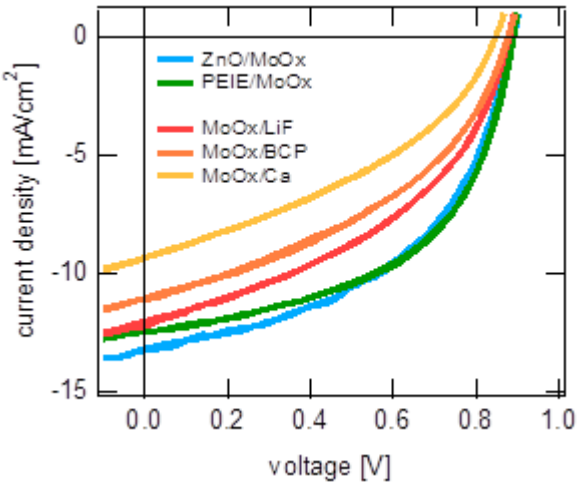

Figure S1. 1-sun *J-V* curves of a PIPCP:$PC_{61}BM$ blend films fabricated with varying device architectures. Inverted devices: ITO/ZnO or PIEIE/PIPCP:$PC_{61}BM$/MoOx/Ag. Conventional devices: ITO/MoOx/PIPCP:$PC_{61}BM$/LiF or BCP or Ca/Al.

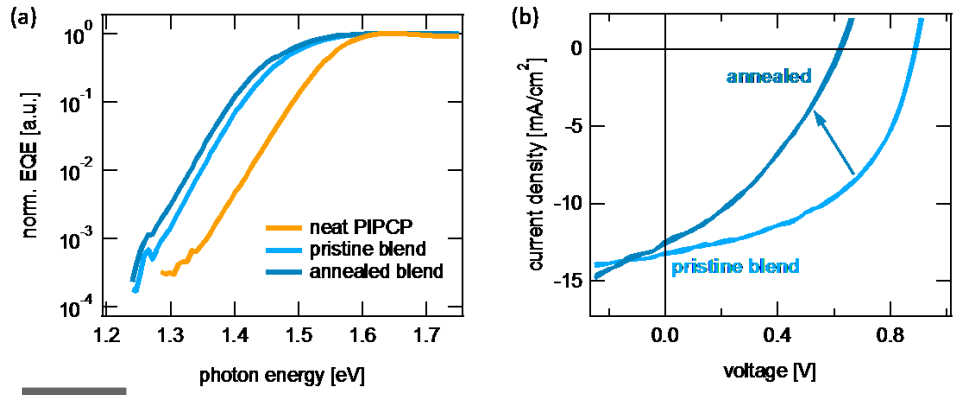

Figure S2. (a) Normalized EQE spectra of neat PIPCP, pristine PIPCP:$PC_{61}BM$, and annealed PIPCP:$PC_{61}BM$ blend films, on a log-lin scale showing the sharp Urbach energy retained in all cases.

(b) 1-sun *J-V* curves of a pristine PIPCP:$PC_{61}BM$ blend film, and a PIPCP:$PC_{61}BM$ blend film annealed at 200°C.

Calculating χ

The cohesive energy density can be decomposed into three Hansen solubility parameters (HSP): dispersive interaction, δ_D, polar interaction, δ_P, and hydrogen bonding interaction, δ_H.

$$CED \equiv \delta_D^{\,2} + \delta_P^{\,2} + \delta_H^{\,2}$$

Accordingly, the χ can be estimated by the following:

$$\chi = \alpha \frac{V_s}{RT}((\delta_{Dp} - \delta_{Ds})^2 + \frac{1}{4}(\delta_{Pp} - \delta_{Ps})^2 + \frac{1}{4}(\delta_{Hp} - \delta_{Hs})^2)$$

Here, V_S is the molar volume of the solvent (herein, PCBM) and α is a correction term which is usually set at 0.5. The HSP can be experimentally determined by solubility studies in multiple solvents. In this study, the HSPs of a given material are calculated by **functional group additive methods**, where the given material is decomposed into functional groups with known HSPs.

$$\delta_d = \frac{\sum F_{di}}{V} \qquad \delta_p = \frac{\sqrt{\sum F_{pi}^{\,2}}}{V} \qquad \delta_h = \sqrt{\frac{\sum E_{hi}}{V}}$$

F_{di}, F_{pi} and F_{hi} correspond to the dispersive interaction, polar interaction, and hydrogen bonding interaction of cohesive energy density, respectively. All contributions to the cohesive energy density can be found in "Properties of polymers, their estimation and correlation with chemical structure", 1976. It is important to consider that the solubility parameter method only considers the collective effect of all functional moieties, without considering the relative arrangement of the functional moieties, such as regioregular or regiorandom arrangements.

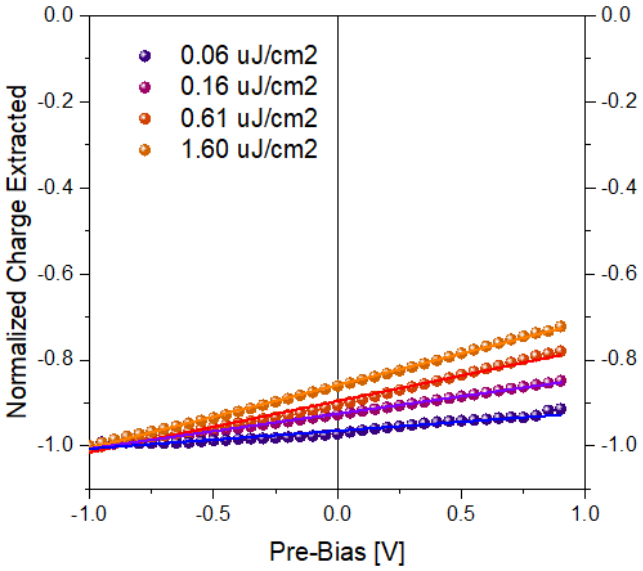

Figure S3. Intensity-dependent TDCF results at 20 ns delay time.

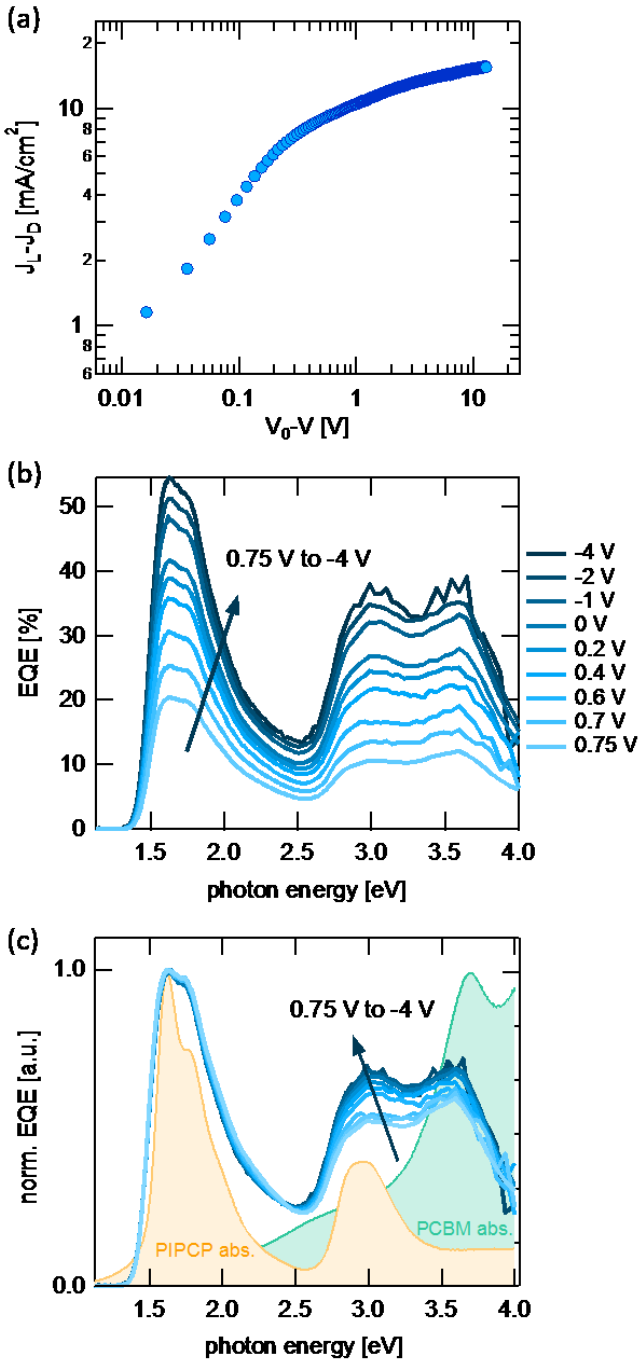

Figure S4. (a) Photocurrent (dark current subtracted from current under illumination) *vs.* the effective bias (applied bias subtracted from the built-in bias) for PIPCP:$PC_{61}BM$. (b) Bias-dependent EQE of PIPCP:$PC_{61}BM$ solar cells. (c) Normalized bias-dependent EQE spectra from (b). Unitless absorption spectra of PIPCP (orange) and $PC_{61}BM$ (green) are shown in the background for reference.

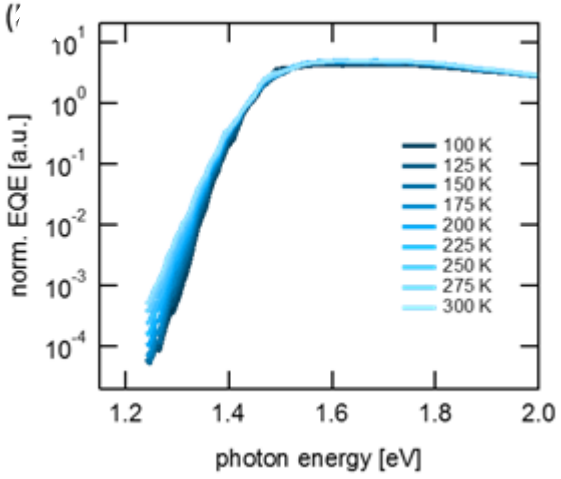

Figure S5. Low-energy tail of the temperature-dependent EQE spectra, showing the sharpening of the Urbach tail with reducing thermal energy.

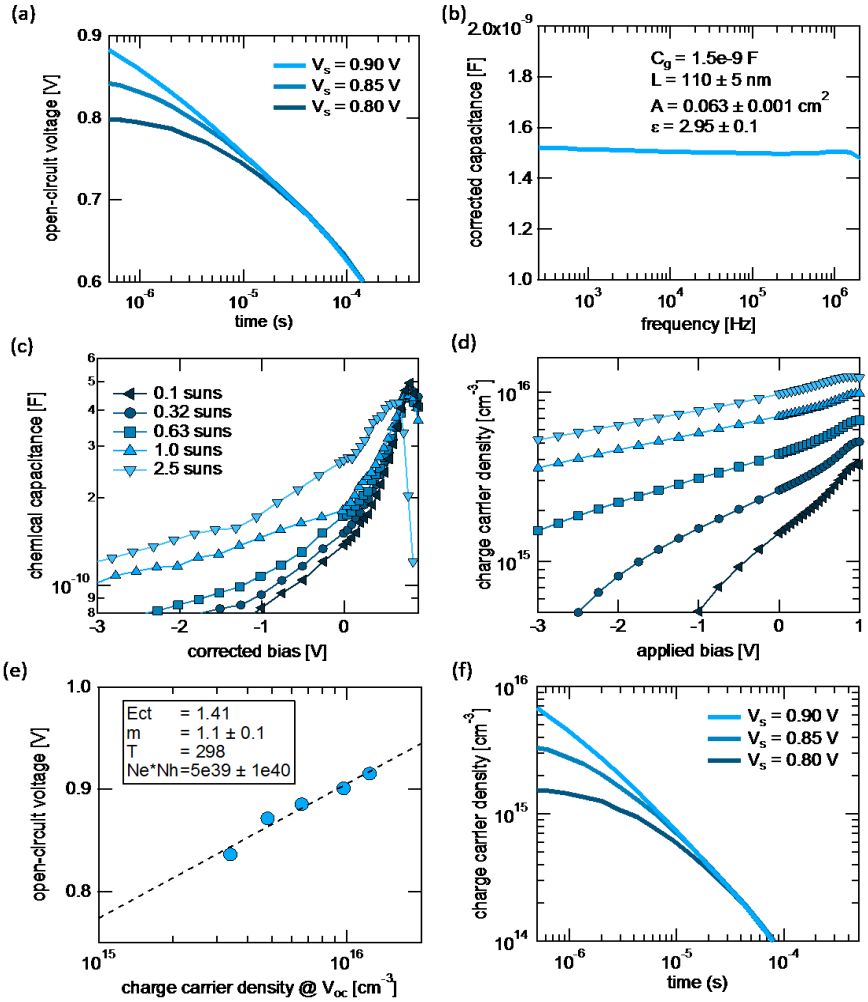

Figure S6. The method to determine k_{rec}. (a) OCVD data for varying light intensities. (b) geometrical capacitance for PIPCP:$PC_{61}BM$ derived from impedance spectroscopy, performed under reverse bias and in the dark to ensure the film is depleted of charge-carriers. (c) Chemical capacitance vs. applied bias, extracted from impedance spectroscopy at different light intensities. (d) Charge carrier density at light intensities corresponding to (c) *vs,* applied bias, obtained from the capacitance data in (c). (e) V_{OC} vs. charge carrier density, obtained by the carrier density (d) and *J-V* measurements at the corresponding light intensities. (f) Carrier density decay dynamics, arrived at by using the relationship in (e) and the V_{OC} decay dynamics from (a).

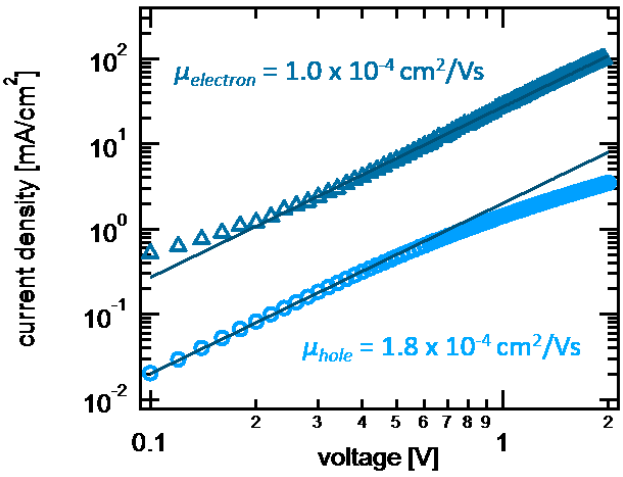

Figure S7. *J-V* curves of hole- and electron-only devices of pristine PIPCP:$PC_{61}BM$, fit to the SCLC model:

$$J = \frac{9}{8}\mu\varepsilon\varepsilon_0\frac{(V - V_{bi})^2}{L^3}$$

Where J is the current density, μ is the SCLC charge carrier mobility, ε is the relative permittivity, ε_0 is vacuum permittivity, V is the applied voltage, V_{bi} is the built-in voltage, and L is the active layer thickness.

Calculating recombination and extraction lifetimes

Using the OCVD data, the recombination life time is determined from the recombination coefficient (k_{rec}) and charge-carrier density at maximum power point (n_{mp}):

$$\tau_{rec} = \frac{1}{kn_{mp}}$$

For comparison, the extraction life time is determined under maximum power point conditions using film thickness (L), charge-carrier mobility (μ), open-circuit voltage (V_{OC}), and voltage at maximum power point (V_{mp}):

$$\tau_{ex} = \frac{L^2}{2\mu(V_{OC} - V_{mp})}$$